

Local Structure of Mott Insulating Iron Oxychalcogenides $\text{La}_2\text{O}_2\text{Fe}_2\text{OM}_2$ ($M = \text{S}, \text{Se}$)

B. Karki,¹ A. Alfailakawi,¹ B. Frandsen,^{2,3} M. S. Everett,⁴ J. C. Neufeind,⁴

Binjie Xu,⁵ Hangdong Wang,⁵ Minghu Fang,^{5,6} and B. Freelon^{1,7*}

¹*Department of Physics, University of Louisville, Louisville, Kentucky 40208, USA*

²*Materials Science Division, Lawrence Berkeley National Laboratory, Berkeley, California 94720, USA*

³*Department of Physics and Astronomy, Brigham Young University, Provo, Utah 84602, USA*

⁴*Spallation Neutron Source, Oak Ridge National Laboratory, Oak Ridge, Tennessee 37831, United States*

⁵*Department of Physics, Zhejiang University, Hangzhou 310027, China*

⁶*Collaborative Innovation Center of Advanced Microstructures, Nanjing University, Nanjing 210093, China*

⁷*Department of Physics and Texas Center for Superconductivity, University of Houston, Texas 77204, USA*

(Dated: March 5, 2022)

We describe the local structural properties of the iron oxychalcogenides, $\text{La}_2\text{O}_2\text{Fe}_2\text{OM}_2$ ($M = \text{S}, \text{Se}$), by using pair distribution function (PDF) analysis and Rietveld refinement methods applied to neutron diffraction data. Our results show that $M = \text{S}$ and Se possess similar nuclear structure at low and room temperatures. The local crystal structures were studied by investigating deviations in atomic positions and the extent of the formation of orthorhombicity. Analysis of the total scattering data suggests that buckling of the Fe_2O plane occurs below 100 K. The buckling may occur concomitantly with a change in octahedral height. Furthermore, within a typical range of 1-2 nm, we observed short-range nematic fluctuations in both of these materials. This finding highlights the ubiquity of nematic fluctuations in iron-based superconductors and related materials.

I. INTRODUCTION

The discovery of superconductivity in iron-based superconductors (FeSCs) has attracted a large amount of attention due to the high transition temperature T_c at which they become superconducting. Although the precise pairing mechanism in these materials remains unknown, it is thought that electron-electron interactions play an important role. Such unconventional superconductivity is in contrast to the conventional electron-phonon coupling [1, 2] present in BCS superconductors. In order to examine the strong-Coulombic postulate for Fe pnictides and chalcogenides, studies were conducted [3–8] to find iron-based Mott insulators that could be driven into the superconducting phase [9, 10]. The iron oxychalcogenides $\text{La}_2\text{O}_2\text{Fe}_2\text{OM}_2$ ($M = \text{S}, \text{Se}$) emerged as a candidate material because they are Mott insulators with structural similarities to the iron pnictides. Several attempts to induce SC in $\text{La}_2\text{O}_2\text{Fe}_2\text{O}(\text{S}, \text{Se})_2$ have been made; however, to date, there are no published reports of SC in these systems [11]. Nevertheless, studying non-superconducting Mott insulators such as $\text{La}_2\text{O}_2\text{Fe}_2\text{OM}_2$ can enhance our understanding of the

Mott insulating region of the iron-chalcogenide electronic phase diagram [1].

Superconductivity in the cuprate superconductors is based on an electron or hole doping of a strongly correlated, Mott insulating phase [12]. Therefore, studying the Mott insulating phase in iron oxychalcogenides might enhance our understanding of the strongly correlated scenarios that lead to high temperature superconductivity [13]. The iron oxychalcogenides $\text{La}_2\text{O}_2\text{Fe}_2\text{OM}_2$ were first reported as antiferromagnetic (AFM) insulators by Mayer et. al. [14]. This layered mixed anion material consists of a body-centered tetragonal crystal structure ($I4/mmm$) with fluorite-like $[\text{La}_2\text{O}_2]^{2+}$ layers and $[\text{Fe}_2\text{O}]^{2+}$ sheets separated by M^{2-} anions [15]. In this structure, $[\text{Fe}_2\text{O}]^{2+}$ consists of an anti- CuO_2 arrangement with an Fe^{2+} cation coordinated by four M^{2-} (above and below the plane) and two in-plane oxygen atoms, forming a tilted Fe-centered FeO_2Se_4 octahedron [13, 14, 16–18]. Fig. 1 shows the crystal structure of $\text{La}_2\text{O}_2\text{Fe}_2\text{OM}_2$ and its octahedra. Structural studies using X-ray [18] and neutron [15] powder diffraction studies did not observe a structural phase transition in $\text{La}_2\text{O}_2\text{Fe}_2\text{O}(\text{S}, \text{Se})_2$. However, an antiferromagnetic ordering was observed at Néel temperatures T_N of 107.2 K and 90.1 K for $\text{La}_2\text{O}_2\text{Fe}_2\text{OS}_2$ and $\text{La}_2\text{O}_2\text{Fe}_2\text{OSe}_2$, respectively. Experiments have indicated the AFM order to be consistent with a 2 - k magnetic structure in which two spin stripe phases are oriented 90° with respect to each other. [15, 16, 19, 20]

Therefore, the structural and magnetic behavior do not have the same correspondence that is observed in some iron-pnictides and iron-chalcogenides in which magnetic and structural phase transitions are coupled. The absence of a structural phase transition in the $\text{La}_2\text{O}_2\text{Fe}_2\text{O}(\text{S}, \text{Se})_2$ Mott insulators motivates us to study

* bkfreelon@uh.edu; Notice: This manuscript has been authored by UT-Battelle, LLC, under contract DE-AC05-00OR22725 with the US Department of Energy (DOE). The US government retains and the publisher, by accepting the article for publication, acknowledges that the US government retains a nonexclusive, paid-up, irrevocable, worldwide license to publish or reproduce the published form of this manuscript, or allow others to do so, for US government purposes. DOE will provide public access to these results of federally sponsored research in accordance with the DOE Public Access Plan (<http://energy.gov/downloads/doe-public-access-plan>).

the local structure to determine whether their short-range lattice symmetries undergo changes. In particular, we are interested in understanding whether local deviations from the average tetragonal structure occur and we seek to characterize lattice or atomic correlations with physical properties.

To date, several studies of FeSCs [21–26] have revealed the presence of a long-range, non-superconducting state called the nematic phase [22] that precedes the superconducting phase transition. The short-range nematic phase, which has been observed in both iron pnictides and iron chalcogenides, develops at a structural phase transition temperature T_s higher than a magnetic transition temperature T_N [27]. The long-range nematic ordering is manifested by spontaneous rotational symmetry breaking while the translational symmetry is preserved [28, 29]. In iron pnictide superconductors symmetry is broken between x and y directions in the Fe-plane [22]. This reduces the rotational point group symmetry from tetragonal to orthorhombic while preserving the translational symmetry. [26, 28]. Nematic ordering was first observed in liquid crystals [30] a long time ago; however, recently quantum analogs of these phases have been discovered in electron fluids. In particular, quantum-Hall systems and many strongly correlated electron systems with very small in-plane structural anisotropy, such as cuprates and pnictides, display very large anisotropies in their physical properties [26, 30]. In the case of iron-based superconductors, the tetragonal symmetry of the normal state is broken, resulting in orthorhombic lattice distortions. Upon doping, the nematic state is suppressed and superconductivity emerges from the broken C_4 rotational symmetry state [31, 32] but often nematic ordering persists into the superconducting state as in LiFeAs [33]. The origin of nematic ordering is not yet fully understood. In the pnictides, it appears to be related to the magnetism, but this may not be the case in iron chalcogenides such as FeSe, which does not show long-range magnetic ordering [27].

Recently, the pair distribution function (PDF) technique [34, 35] has been used to study the local atomic arrangement and structural nematic fluctuations in iron-based superconductors for both normal and superconducting phases. PDF methods can be used to measure local scale deviations from the global crystal symmetry of a material [22, 36]. In FeSe_{1-x}Te_x systems, PDF investigated the reduction of local crystal symmetry which enhances the local moment formation leading to magnetic instability [37]. X-ray and neutron PDF on FeSe and (Sr, Na)Fe₂As₂ revealed the presence of short-range orthorhombic distortions at temperatures well above the static nematic and orthorhombic ordering temperature T_s [28, 29, 32, 36]. The observation of nematic fluctuations in iron-based superconductors, by using neutron and x-ray PDF analysis, provided evidence that nematic degrees of freedom exist near the superconducting phase [28]. Horigane et. al [38] conducted PDF studies of La₂O₂Fe₂OS₂ local structure and found a large

anisotropic thermal displacement parameter for the O(2) atom along the c -axis (U_{33}). That study concluded that the crystal structure is strongly coupled to the magnetism in this system.

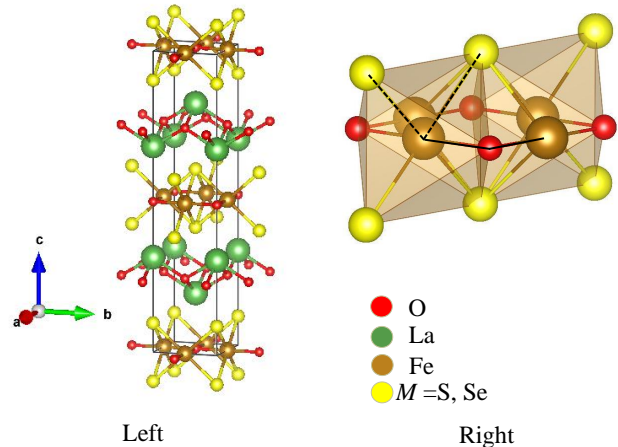


FIG. 1. The crystal structure of La₂O₂Fe₂OM₂ ($M = S, Se$) is shown in the left panel. The right panel shows FeO₂Se₄ octahedra, where the Fe atom is surrounded by four $M = S, Se$ atoms and two O(2) atoms. Black solid lines show the angle formed by Fe-O-Fe atoms while the dashed lines show M -Fe- M angle.

We report the use of the neutron pair distribution function (PDF) technique to study the local structure of La₂O₂Fe₂O(S, Se)₂ and to investigate the relationship between the structure and magnetism. The experimental methods are discussed in Section II, the results of this study are presented in Section III, section IV includes the discussion and the conclusions are presented in section V. Our results indicate the presence of short-range orthorhombic distortions suggestive of short-range nematicity in both materials La₂O₂Fe₂O(S, Se)₂, despite the persistence of tetragonal symmetry in the average structure at all temperatures. We discuss the behavior of these fluctuations as a function of temperature. It appears that the change in the chalcogen from S to Se does not affect this behavior.

II. EXPERIMENTAL METHODS

1. Synthesis

La₂O₂Fe₂O(S, Se)₂ samples were prepared by a solid-state reaction method [14] from stoichiometric amounts of high purity La₂O₃, S, Se, and Fe powders. The appropriate mixture of these powders was grounded thoroughly, pelletized then heated in an evacuated quartz tube at 1030° C for 72 hours. This process was repeated three times. After being pulverized into fine powders, lab-based x-ray powder diffraction showed the materials to be of the high-quality and single phase [13–15].

2. Neutron Powder Diffraction

Time-of-flight (TOF) neutron powder diffraction measurements were performed at the POWGEN diffractometer of the Spallation Neutron Source (SNS) at Oak Ridge National Laboratory (ORNL). Five grams of $\text{La}_2\text{O}_2\text{Fe}_2\text{OS}_2$ and 4.5 g of $\text{La}_2\text{O}_2\text{Fe}_2\text{OSe}_2$ powders were placed in vanadium cans. Seven measurements at the temperatures 10, 50, 100, 150, 200, 250 and 300 K were performed, on each sample, for approximately one hour. The center wavelength and d -spacing range of neutrons in this experiment were 1.5 Å and 0.49664-13.50203 Å respectively. Rietveld refinements were conducted using GSAS-II software [39].

3. Pair Distribution Function

Neutron total scattering data were collected using the Nano-scale Ordered Materials Diffractometer (NOMAD) beamline at the SNS in ORNL. $\text{La}_2\text{O}_2\text{Fe}_2\text{O}(\text{S}, \text{Se})_2$ powders were loaded and sealed in the vanadium cans inside a glove-box and were placed in an orange cryostat. A total of sixteen measurements were performed on each sample at various temperatures ranging from 2 K to 300 K. A higher number of data points were taken, in small steps, around the Néel temperature. Data were collected for approximately two hours at each temperature. In order to obtain structural information relevant to the samples, an empty vanadium sample can was measured for two hours for background subtraction.

The reduced pair distribution function (PDF) $G(r)$ is obtained experimentally by Fourier transforming the total scattering data as follows:

$$G(r) = \frac{2}{\pi} \int_{Q_{\min}}^{Q_{\max}} Q(S(Q) - 1) \sin(Qr) dQ, \quad (1)$$

Where $S(Q)$ is the normalized structure factor, and Q is the scattering vector, defined as $Q = \frac{4\pi \sin(\theta)}{\lambda}$ in which λ and θ are the neutron wavelength and scattering angle, respectively. PDF data were refined and analyzed using PDFGUI [35] program and DIFFPY-CMI [40] suite. The calculated reduced pair distribution function $G_c(r)$ is obtained from the structural model using equation (2) [41].

$$G_c(r) = \frac{1}{r} \sum_i \sum_j \left[\left(\frac{b_i b_j}{\langle b \rangle^2} \right) \delta(r - r_{ij}) \right] - 4\pi r \rho_0 \quad (2)$$

where b_i , b_j and $\langle b \rangle$ are the average scattering power of constituent atoms of the sample. The summation is over all atoms i and j in the model, where the distance separating any given pair of atoms is r_{ij} .

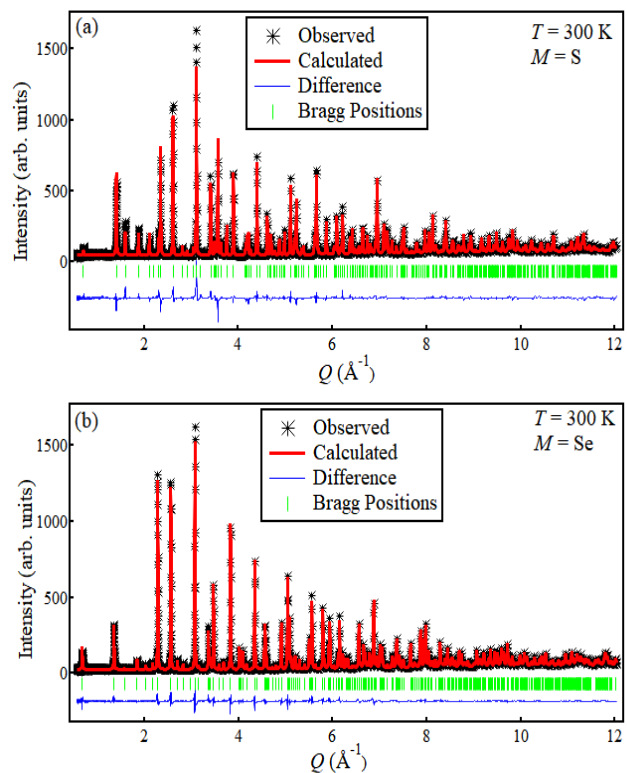


FIG. 2. Neutron Rietveld refinement of the nuclear model of a) $M = \text{S}$ and b) $M = \text{Se}$ at 300 K as a function of momentum transfer Q . The details of the fit are provided in the text.

III. RESULTS

A. Crystal Structure and Lattice Parameters

We confirmed the crystal structure of our samples through the neutron powder diffraction. The Rietveld refinement of neutron powder diffraction data was performed using GSAS II software [39]. Fig. 2(a) and (b) show the Rietveld refinement of neutron powder diffraction data measured at 300 K using neutrons of central wavelength 1.5 Å. Both $M = \text{S}, \text{Se}$ materials show similar nuclear structures having space group $I4/mmm$ (space group No. 139) which is consistent with the previous studies [14, 15]. Our findings show that the lattice parameters of $\text{La}_2\text{O}_2\text{Fe}_2\text{OSe}_2$ ($a = 4.0887(5)$ Å, $c = 18.6081(3)$ Å) is larger than that of the $\text{La}_2\text{O}_2\text{Fe}_2\text{OS}_2$ ($a = 4.0439(9)$ Å, $c = 17.8945(6)$ Å), as expected for the larger Se atoms. Rietveld refinement parameters of both $M = \text{S}, \text{Se}$ are tabulated in Table I including lattice parameters (a and c) as well as the anisotropic thermal displacement parameters U_{33} for all atoms. It was observed that U_{33} for O(2) site is much larger than all the other sites. The quality of the presented fits was characterized by the listed Rietveld parameters: R -whole pattern R_w , crystallographic factor R_F and goodness of fit tabulated in Table I.

	La ₂ O ₂ Fe ₂ OSe ₂	La ₂ O ₂ Fe ₂ OS ₂
a (Å)	4.0887(5)	4.0439(9)
c (Å)	18.6081(3)	17.8945(0)
La - U_{33} (Å ²)	0.00722	0.01718
Fe - U_{33} (Å ²)	0.01077	0.02258
O(1) - U_{33} (Å ²)	0.00998	0.02049
O(2) - U_{33} (Å ²)	0.02226	0.04643
M - U_{33} (Å ²)	0.00522	0.02124
Volume (Å ³)	311.08(8)	292.64(1)
Space Group	I_4/mmm	I_4/mmm
R_w (%)	6.79	6.79
R_F (%)	2.75	6.57
Goodness of fit	5.37	6.57

TABLE I. Refined parameters from Rietveld analysis of neutron powder diffraction data of La₂O₂Fe₂O(S, Se)₂ at $T = 300$ K.

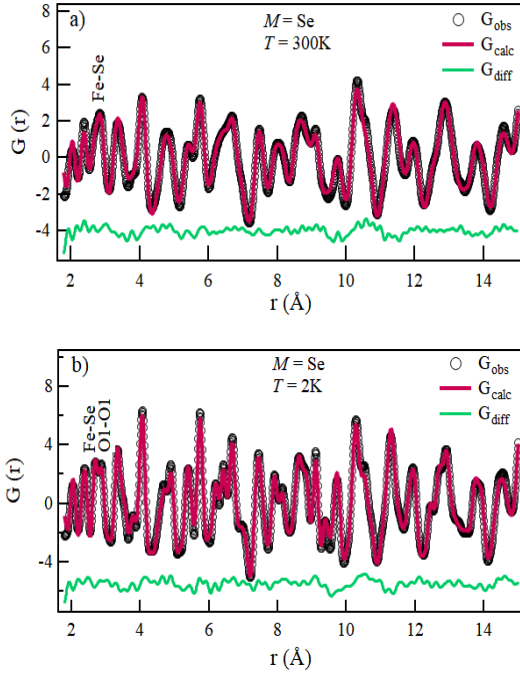


FIG. 3. PDF refinement plot of $M = \text{Se}$ at a) 300 K and b) 2 K within the range of $1.8 \text{ Å} \leq r \leq 10.0 \text{ Å}$. Observed and calculated PDF patterns are represented by G_{obs} (black) and G_{calc} (red), respectively, with the difference profile by G_{diff} (green).

Having obtained a confirmation of the global lattice symmetry for our samples, we then investigated the local symmetry [28, 32, 42–45]. The local structure data of La₂O₂Fe₂OM₂ ($M = \text{S, Se}$) was analyzed by using the PDF refinement program PDFGUI [35] to determine the localized structural arrangement as a function of temperature and length scale. During the refinement process the lattice parameter, scale factor, atomic positions, and the thermal parameters were fitted. In order to allow for local orthorhombic symmetry breaking, we parameterized the lattice constants as $a = a_{\text{mid}}(1 + \delta)$ and $b = a_{\text{mid}}(1 - \delta)$,

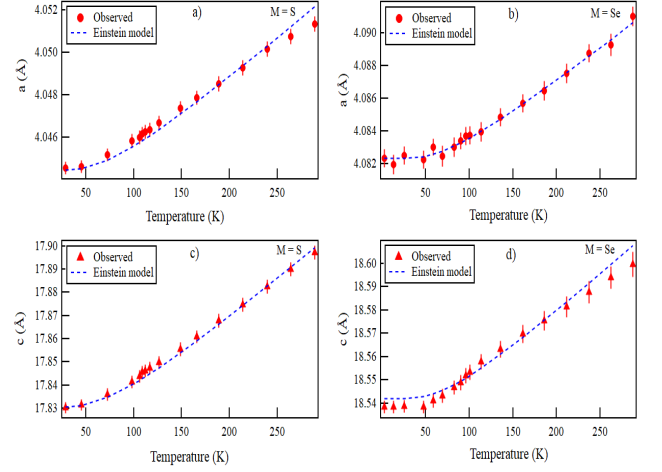


FIG. 4. Lattice parameters as a function of temperature for $M = \text{S, Se}$ determined from temperature-series sequential PDF refinement. a) a - and c) c -lattice parameter are shown for $M = \text{S}$ and b) a - and d) c -lattice parameter are shown for $M = \text{Se}$. Blue dotted lines represent an Einstein model of lattice thermal expansion (see text).

where $a_{\text{mid}} = \frac{a+b}{2}$ and $\delta = \left| \frac{a-b}{a+b} \right|$. All refinements were performed on the Nyquist grid. Instrumental parameters q_{damp} and q_{broad} , which are the parameters that correct the PDF envelope function [46, 47] for the instrument resolution [35, 41], were fixed by using an independent measurement of a standard Si sample.

In Fig. 3, refined PDF data is presented for La₂O₂Fe₂O(S, Se)₂. The observed data G_{obs} is shown in black and the calculated data G_{calc} is shown in red, while the difference between the observed data and the calculated data, G_{diff} , is shown in green. We observed that the third peak of Fig. 3a, representing a Fe-Se distance of 2.7 Å at 300 K, shows a clear modification into Fe-Se at 2.67 Å and O(1)-O(1) at 2.87 Å at low temperature (see Fig. 3b). The peak change indicates two slight changes of Fe and O positions that affect the associated interatomic positions. The implications of these atomic displacements are discussed below.

The lattice constants were obtained as a function of temperature using PDF analysis. Fig. 4 shows the temperature dependence of the lattice parameters a and c for both La₂O₂Fe₂O(S, Se)₂ samples in the range of 1.8 to 49.99 Å, where the data are fitted using an Einstein model of thermal expansion. Following previous work [18], the Einstein fitting model was calculated using equations (3) and (4) under the assumption that the thermal expansion is proportional to the internal energy of a quantum mechanical oscillator [48]. Fig. 4 also shows that the lattice parameter a increases with increasing temperature and fits well with the Einstein model of thermal expansion [48]. However, the lattice parameter c shows a kink near 90 K in the case of $M = \text{Se}$ (see

discussion).

$$a(T) = a_0 \left[1 + \alpha \theta_E f_E \left(\frac{\theta_E}{T} \right) \right] \quad (3)$$

$$f_E \left(\frac{\theta_E}{T} \right) = \frac{1}{\exp(\frac{\theta_E}{T}) - 1} \quad (4)$$

Here, a is the lattice constant, a_0 is the lattice constant at 0 K, α is the high temperature thermal expansion coefficient, and θ_E is the characteristic Einstein temperature. In our plots, we have used $\theta_E = 211$ K as reported by Free *et al.* [18].

B. Temperature Dependence of Thermal Displacement Parameters

Fig. 5 shows the temperature dependence of the anisotropic thermal displacement parameters U_{11} and U_{33} for both $M = S, \text{Se}$. We note the relatively high values of U_{11} parameter for the $M = S, \text{Se}$ sites and the U_{33} parameter for the O(2) site. The large U_{33} parameter for the O(2) site agrees well with the neutron powder diffraction results (See Table I). The large an anisotropic thermal displacement parameter U_{33} corresponds to O(2) displacement above and below the Fe_2O plane. This particular displacement can be accompanied by a distortion of Fe-O-Fe angle (See Fig. 1 where this angle is highlighted by a solid black line in the octahedra). Another possible movement along the c -axis is that of sulfur/selenium atoms with respect to the Fe atoms in the octahedra. This motion would affect the M -Fe- M angle in the octahedra (See Fig. 1 where this angle is highlighted by dashed black lines in the octahedra).

Fig. 6 provides views of the atomic displacements under discussion. Panel a) shows a view along the a -axis while panel b) provides an isometric perspective view by presenting slight rotations about the a and c crystal axes. In panel b) black solid lines show the Fe atom movement and black dashed line shows the movement of O(2) atom. When the O(2) atoms in the Fe_2O plane move up or down the angle Fe-O-Fe changes causing buckling of the Fe_2O plane. O(2) atoms are displacing out of the plane by ~ 0.015 Å. Allowing the z -coordinates of the two O(2) atoms to displace opposite to each other results in the U_{33} parameter for the O(2) site dropping down to a value that is in line with other atomic sites. This result suggests that local buckling of the Fe_2O plane may occur through small displacements of the O(2) atom above and below the plane.

C. Local Orthorhombicity

The use of pre-written macros allows PDFGUI to fit data sets through a series of boxcar refinements that differ one from another by corresponding fitting ranges [49].

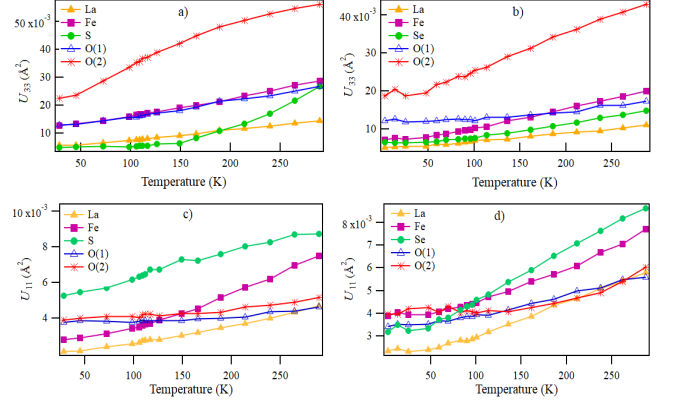


FIG. 5. The temperature dependence of the anisotropic thermal displacement parameters a) U_{33} and c) U_{11} for $M = S$; and b) U_{33} and d) U_{11} for $M = \text{Se}$ for all atomic sites.

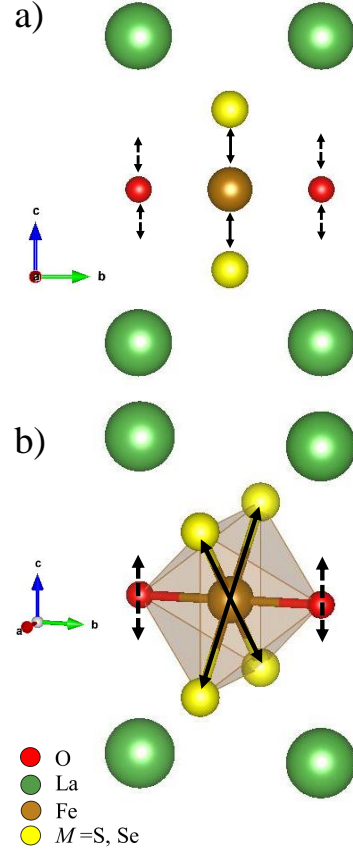


FIG. 6. Panel (a) shows possible Fe and Se/S atomic movement within the $\text{La}_2\text{O}_2\text{Fe}_2\text{O}(\text{S}, \text{Se})_2$ octahedra that result in the buckling of the Fe_2O plane. (b) The dashed lines show Fe atom movement in the Fe_2O plane and the solid lines show Fe movement with respect to M .

Since we have performed PDF data sets over a wide range of temperatures, we used PDFGUI T -series and r -series macros to study details of the local to aver-

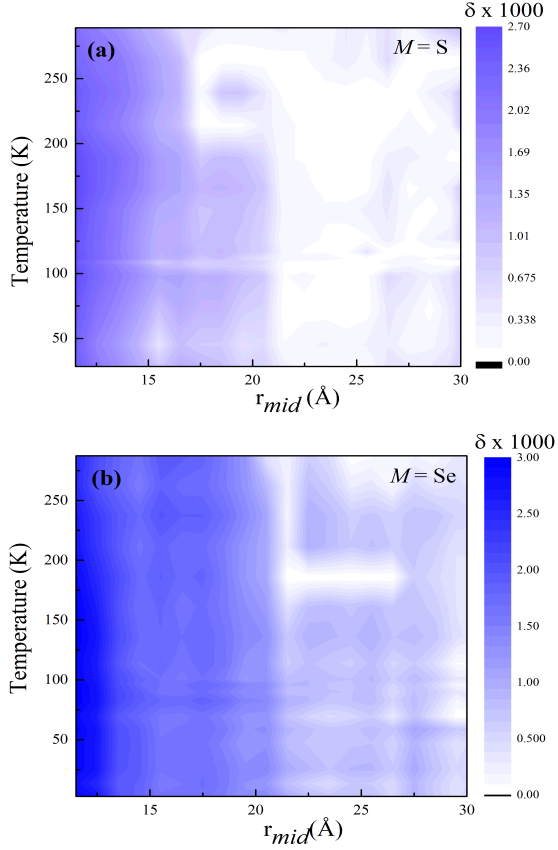


FIG. 7. Color maps of the refined orthorhombicity determined from neutron PDF analysis for a) $M = S$ and b) $M = Se$.

age structure crossover in our materials. These macros allow the setup of boxcar fits, in which the same model is fitted over different real space intervals (r - ranges) for different temperatures of the PDF data [50]. We have performed extensive T - and r - series PDF fits to determine the atomic structure as a function of temperature and length scale [28]. The evolution of the orthorhombicity of the local structure (short-range) to the average structure (long range) is presented in the color maps of Fig. 7. The most relevant structural parameter for the local distortion is the orthorhombicity. Color maps of orthorhombicity were prepared, for both $M = S$ and Se by using the results of T - and r - series refinements based on the orthorhombic symmetry. We did the T - series refinement by performing the PDF fits on low temperature data at first, then we run the sequential PDF fits for all of our data collected at various temperatures. For each temperature data, we have performed the r - series refinement in a sliding 20 Å data window from [1.5 - 21.5 Å] to [29.5 - 49.5 Å] in 1 Å steps, resulting in 29 fits per temperature. Orthorhombicity and c lattice parameter were extracted from all of these fits for all temperatures to produce the color maps. Color maps were made using the ORIGIN software [51]. In these color maps, the midpoint of the fitting range r_{mid} is shown on the x-axis, the

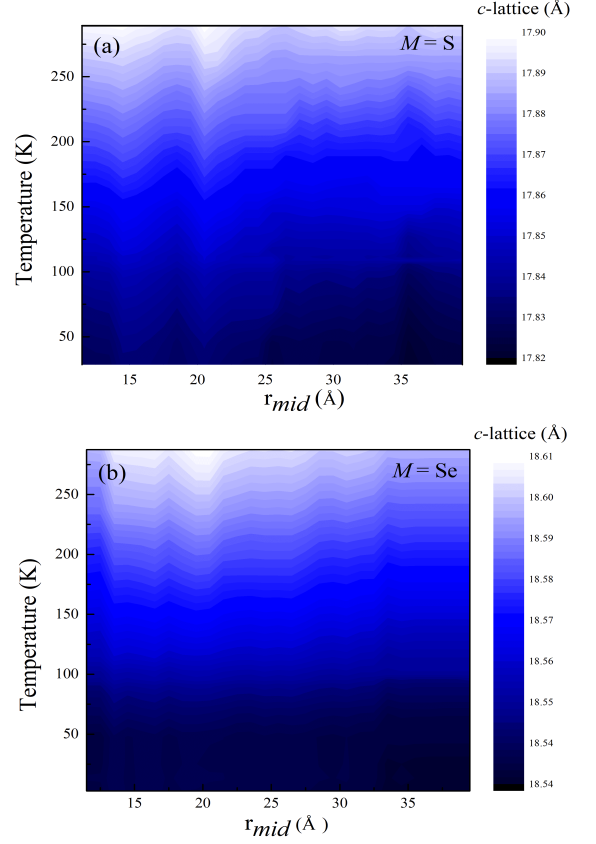


FIG. 8. Color maps of c -lattices for $La_2O_2Fe_2O(S, Se)_2$ derived from T - and r -series PDF refinements for a) $M = S$ and b) $M = Se$.

temperature is shown on the y-axis, and orthorhombicity is shown on the color bar as indicated by the brightness of the colors from light blue to dark blue. The dark blue color denotes high orthorhombicity, light blue represent zero orthorhombicity *i.e.*, tetragonality. The maps indicate that at short ranges, over all temperatures, the presence of orthorhombicity is observed, but it diminishes over longer length scales.

Fig. 9 presents the local orthorhombicity δ as a function

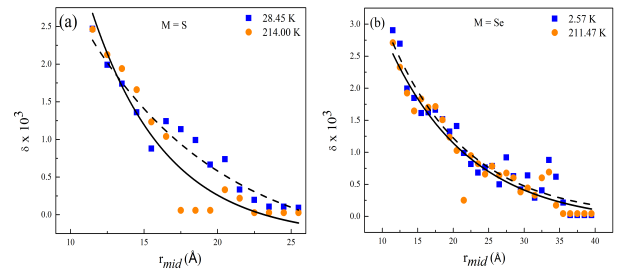


FIG. 9. Orthorhombicity as a function of fitting range for a) $M = S$ and b) $M = Se$ at low and high temperature.

of the midpoint of the fitting ranges for two representative temperatures. Data were fitted with exponential

decay functions. Fig. 9(a) shows the orthorhombicity of $M = S$ at 28.45 K and 214.0 K. At both temperatures, the orthorhombicity is largest at short fitting ranges and gradually decreases to form a plateau at larger fitting ranges. A black solid (dashed) line shows the exponential fitting function for 28.45 K (214.0 K) with decay lengths of $6.42 \pm 2.2 \text{ \AA}$ ($3.52 \pm 0.93 \text{ \AA}$), respectively. Fig. 9(b) displays the orthorhombicity at different fitting ranges for $M = Se$ at temperature 2.57 K and 211.47 K. Black solid (dashed) line shows the exponential fitting function for 2.57 K (211.47 K) with decay length of $7.52 \pm 1.38 \text{ \AA}$ ($7.92 \pm 1.6 \text{ \AA}$), respectively. Figs. 9(a) and (b) provided evidence of the greater orthorhombicity at shorter ranges.

The color maps of the c -lattice parameter for $M = S, Se$ determined from T - and r -series refinement of pair distribution function analysis are presented in Fig. 8. In this figure, the x-axis is the midpoint of fitting range r_{mid} , the y-axis is the temperature, and the color bar shows the c -lattice parameter with light blue for the high intensity and black for low intensity. c -lattice color maps show the evolution of c -lattice from the local structure (short-range) to the average structure (long range). For both $La_2O_2Fe_2O(S, Se)_2$ materials, we can see an increase in the c -lattice as the temperature increases overall r_{mid} ranges.

IV. DISCUSSION

Neutron powder diffraction experiments confirmed the average crystal structure of $La_2O_2Fe_2O(S, Se)_2$ as tetragonal systems with space group ($I4/mmm$) (see Fig. 2) in agreement with the previous studies on these materials [13–18]. Unlike many iron pnictides which undergo a structural phase transition from tetragonal to orthorhombic symmetries near T_s , $La_2O_2Fe_2O(S, Se)_2$ lattice symmetries are not observed to change with temperature. However, both $La_2O_2Fe_2O(S, Se)_2$ undergo a magnetic transitions from paramagnetic (PM) phases to antiferromagnetic (AFM) phases at respective Néel temperatures T_N . Neutron powder diffraction (Fig. 5 and Table I) showed that the thermal displacement parameter for the O(2) atom along the c -axis was larger than all the other thermal displacement parameters. This was the finding for both materials $M = S$ and Se .

In order to probe the local structure, we employed the neutron PDF technique to investigate the local changes in the atomic positions and c -axes of $La_2O_2Fe_2O(S, Se)_2$. The PDF analysis revealed similar thermal displacement behavior on short length scales. In addition, the temperature dependence of the c -lattice parameter showed a kink near the Néel temperature for $M = Se$ (see Fig. 4). However, no discontinuity was observed in the case of $M = S$. Such a finding is consistent with previous reports of c -lattice discontinuities in oxyselenides [18, 52, 53] and the less prominent occurrence of this behavior in the oxysulfides [17]. The discontinuities were attributed to magne-

tostrictive effects in the oxyselenides. In the case of oxysulfides, a relatively reduced amount of c -lattice discontinuity was argued to be due to shorter c -lattices [17]. According to Horigane et al. [38] deviations in the c -lattice parameter from the average crystallographic structure are due to the fact that the thermal displacement parameter U_{33} for O(2) along the c -axis grows rapidly with the increase in temperature. A similar O(2) trend, in $SrFeO_2$ [54], was reported to be related to Fe_2O planar buckling.

For $La_2O_2Fe_2O(S, Se)_2$, the buckling of the Fe_2O plane may occur when there is distortion in either the Fe or O(2) sites. In the case of $M = Se$, a high U_{33} value for O(2) (see Fig. 5) suggests that the largest distortions should occur for that site. A distortion in the Fe site can lead to two Fe-Se correlations since each Fe atom is surrounded by four Se atoms of the octahedra (see Fig. 6b). Therefore, the modification observed in Fe-Se correlation peak (the third peak of see Fig. 3a) might indicate a subtle distortion in the Fe site. Overall, these findings for $M = Se$ suggest that there is a distortion either in the Fe or O(2) sites, and both implicated as possible reasons for Fe_2O buckling.

Our analysis of the local structure of $La_2O_2Fe_2O(S, Se)_2$ reveals the presence of short-range orthorhombic distortions on a length scale of 1 - 2 nm over a temperature range from 2 - 300 K. These distortions are very similar to those found in FeSe [32, 36] and $(Sr, Na)Fe_2As_2$ [28, 29], which have been attributed to short-range nematic fluctuations that persist up to temperatures well above the magnetic and/or structural transition temperatures. Given the structural and magnetic similarities between these iron oxychalcogenides and the superconducting iron pnictides and chalcogenides, we suggest that the local orthorhombicity observed here is likewise related to fluctuating, short-range nematic distortions.

The occurrence of such fluctuations across a variety of pnictide superconductors and the incoherent electronic systems presented here raise the question of how critical nematic fluctuations are to the superconducting mechanism. This specific inquiry has become the key focal point of the field of iron-based high- T_c superconductivity. In most FeSCs, superconductivity is found in close proximity to a magnetically ordered state. However, there is a nematic, non-superconducting state besides magnetism at a specific temperature T_{nem} . Nematic ordering has been systematically observed in iron pnictide and chalcogenide superconductors. The short-range nematic fluctuations, which are deviations from the average structure, may provide the information about the origin of nematicity and its relation to superconductivity mechanism [32, 36, 55–60]. In FeSCs and other related materials, significant information can be gained from the nematic phase which occurs near T_s and from the nematic fluctuations that occur over a large range of temperatures.

The fact that nematic degrees of freedom appear to be active in these Mott insulating, non-superconducting iron oxychalcogenides highlights the ubiquity of nematic-

ity for layered iron-based systems. It also suggests that active nematic degrees of freedom are not sufficient to guarantee superconductivity, although they may well be necessary. It may be the case that nematic fluctuations and another phase must conspire to produce high-temperature superconductivity in iron-based systems.

V. CONCLUSIONS

The local structure of Mott insulating iron oxychalcogenides was studied using neutron powder diffraction and pair distribution techniques. Neutron powder diffraction showed a similar nuclear structure of $M = \text{Se}$ and S with the only difference in the atomic radii of two chalcogens. Pair distribution function analysis indicated the presence of the local distortion between tetragonal and orthorhombic symmetry. These findings suggest the presence of short-range local distortion with a typical length scale of 1 - 2 nm in both of these materials.

VI. ACKNOWLEDGMENTS

The authors would like to thank the University of Louisville for funding support. Alfaiakawi would like to thank Kuwait University for supporting this work through a graduate scholarship. Work at University of Houston was supported by the State of Texas through TcSUH. The research in ZJU is supported by the Ministry of Science and Technology of China under Grants No. 2016YFA0300402 and No. 2015CB921004 and the National Natural Science Foundation of China (NSFC) (No. 11974095, 11374261), and the Fundamental Research Funds for the Central Universities. This work used resources of the Spallation Neutron Source, a DOE office of Science User Facility operated by the Oak Ridge National Laboratory.

-
- [1] Q. Si, R. Yu, and E. Abrahams, *Nature Reviews Materials* **1**, 16017 (2016).
 - [2] J. Paglione and R. L. Greene, *Nature Physics* **6**, 645 (2010).
 - [3] L. Zhao, D. Wang, Q. Huang, H. Wu, R. Sun, X. Fan, Y. Song, S. Jin, and X. Chen, *Physical Review B* **99**, 094503 (2019).
 - [4] T. Yildirim, *Phys. Rev. Lett.* **102**, 037003 (2009).
 - [5] Q. Si and E. Abrahams, *Phys. Rev. Lett.* **101**, 076401 (2008).
 - [6] B. Mansart, D. Boschetto, A. Savoia, F. Rullier-Albenque, F. Bouquet, E. Papalazarou, A. Forget, D. Colson, A. Rousse, and M. Marsi, *Phys. Rev. B* **82**, 024513 (2010).
 - [7] S. Lee, S. Roh, Y.-S. Seo, M. Lee, E. Jung, J. M. Ok, M.-C. Jung, B. Kang, K.-W. Lee, J. S. Kim, *et al.*, *Journal of Physics: Condensed Matter* **31**, 445602 (2019).
 - [8] C. H. Wong and R. Lortz, *arXiv preprint arXiv:1902.06463* (2019).
 - [9] E. Abrahams and Q. Si, *Journal of physics: Condensed matter* **23**, 223201 (2011).
 - [10] S. K. Shrivastava and G. Kumar, *International Journal of Emerging Technologies and Innovative Research* **6**, 417 (2019).
 - [11] S. Landsgesell, K. Prokeš, T. Hansen, and M. Frontzek, *Acta Materialia* **66**, 232 (2014).
 - [12] P. A. Lee, N. Nagaosa, and X.-G. Wen, *Rev. Mod. Phys.* **78**, 17 (2006).
 - [13] J.-X. Zhu, R. Yu, H. Wang, L. L. Zhao, M. D. Jones, J. Dai, E. Abrahams, E. Morosan, M. Fang, and Q. Si, *Phys. Rev. Lett.* **104**, 216405 (2010).
 - [14] J. M. Mayer, L. F. Schneemeyer, T. Siegrist, J. V. Waszczak, and B. Van Dover, *Angewandte Chemie International Edition in English* **31**, 1645 (1992).
 - [15] B. Freelon, Z. Yamani, I. Swainson, R. Flacau, B. Karki, Y. H. Liu, L. Craco, M. S. Laad, M. Wang, J. Chen, R. J. Birgeneau, and M. Fang, *Phys. Rev. B* **99**, 024109 (2019).
 - [16] E. E. McCabe, C. Stock, E. E. Rodriguez, A. S. Wills, J. W. Taylor, and J. S. O. Evans, *Phys. Rev. B* **89**, 100402 (2014).
 - [17] R. K. Oogarah, E. Suard, and E. E. McCabe, *Journal of Magnetism and Magnetic Materials* **446**, 101 (2018).
 - [18] D. G. Free and J. S. O. Evans, *Phys. Rev. B* **81**, 214433 (2010).
 - [19] C. Stock and E. E. McCabe, *Journal of Physics: Condensed Matter* **28**, 453001 (2016).
 - [20] M. Günther, S. Kamusella, R. Sarkar, T. Goltz, H. Luetkens, G. Pascua, S.-H. Do, K.-Y. Choi, H. D. Zhou, C. G. F. Blum, S. Wurmehl, B. Büchner, and H.-H. Klauss, *Phys. Rev. B* **90**, 184408 (2014).
 - [21] P. Dai, J. Hu, and E. Dagotto, *Nature Physics* **8**, 709 (2012).
 - [22] R. M. Fernandes, A. V. Chubukov, and J. Schmalian, *Nature Physics* **10**, 97 (2014).
 - [23] J.-H. Chu, H.-H. Kuo, J. G. Analytis, and I. R. Fisher, *Science* **337**, 710 (2012).
 - [24] J. Li, P. J. Pereira, J. Yuan, Y.-Y. Lv, M.-P. Jiang, D. Lu, Z.-Q. Lin, Y.-J. Liu, J.-F. Wang, L. Li, *et al.*, *Nature communications* **8**, 1880 (2017).
 - [25] R. M. Fernandes and A. J. Millis, *Physical review letters* **111**, 127001 (2013).
 - [26] E. Fradkin, S. A. Kivelson, M. J. Lawler, J. P. Eisenstein, and A. P. Mackenzie, *Annu. Rev. Condens. Matter Phys.* **1**, 153 (2010).
 - [27] A. V. Chubukov, R. M. Fernandes, and J. Schmalian, *Physical Review B* **91**, 201105 (2015).
 - [28] B. A. Frandsen, K. M. Taddei, D. E. Bugaris, R. Stadel, M. Yi, A. Acharya, R. Osborn, S. Rosenkranz, O. Chmaissem, and R. J. Birgeneau, *Phys. Rev. B* **98**, 180505 (2018).
 - [29] B. A. Frandsen, K. M. Taddei, M. Yi, A. Frano, Z. Guguchia, R. Yu, Q. Si, D. E. Bugaris, R. Stadel, R. Osborn, S. Rosenkranz, O. Chmaissem, and R. J.

- Birgeneau, Phys. Rev. Lett. **119**, 187001 (2017).
- [30] S. Okamoto, D. Sénéchal, M. Civelli, and A.-M. S. Tremblay, Phys. Rev. B **82**, 180511 (2010).
 - [31] Y. Kushnirenko, D. Evtushinsky, T. Kim, I. Morozov, L. Harnagea, S. Wurmehl, S. Aswartham, A. Chubukov, and S. Borisenko, arXiv preprint arXiv:1810.04446 (2018).
 - [32] R. J. Koch, T. Konstantinova, M. Abeykoon, A. Wang, C. Petrovic, Y. Zhu, E. S. Bozin, and S. J. L. Billinge, Phys. Rev. B **100**, 020501 (2019).
 - [33] C. M. Yim, C. Trainer, R. Aluru, S. Chi, W. N. Hardy, R. Liang, D. Bonn, and P. Wahl, Nature Communications **9**, 2602 (2018).
 - [34] T. Egami and S. J. L. Billinge, *Underneath the Bragg Peaks: Structural Analysis of Complex Materials* (Pergamon Press Elsevier, Oxford, England, 2003).
 - [35] C. L. Farrow, P. Juhas, J. W. Liu, D. Bryndin, E. S. Božin, J. Bloch, T. Proffen, and S. J. L. Billinge, Journal of Physics: Condensed Matter **19**, 335219 (2007).
 - [36] B. A. Frandsen, Q. Wang, S. Wu, J. Zhao, and R. J. Birgeneau, Phys. Rev. B **100**, 020504 (2019).
 - [37] D. Louca, K. Horigane, A. Llobet, R. Arita, S. Ji, N. Katayama, S. Konbu, K. Nakamura, T.-Y. Koo, P. Tong, and K. Yamada, Phys. Rev. B **81**, 134524 (2010).
 - [38] K. Horigane, K. Kawashima, S. Ji, M. Yoshikawa, D. Louca, and J. Akimitsu, in *Proceedings of the International Conference on Strongly Correlated Electron Systems (SCES2013)* (2014) p. 015039.
 - [39] B. H. Toby and R. B. Von Dreele, Journal of Applied Crystallography **46**, 544 (2013).
 - [40] P. Juhás, J. N. Louwen, L. van Eijck, E. T. C. Vogt, and S. J. L. Billinge, Journal of Applied Crystallography **51**, 1492 (2018).
 - [41] T. Proffen and S. J. L. Billinge, Journal of Applied Crystallography **32**, 572 (1999).
 - [42] C. E. White, J. L. Provis, T. Proffen, and J. S. Van Deventer, Journal of the American Ceramic Society **93**, 3486 (2010).
 - [43] M. Paściak, P. Ondrejčovic, J. Kulda, P. Vaněk, J. Drahošoupil, G. Steciuk, L. Palatinus, T. Welberry, H. Fischer, J. Hlinka, *et al.*, Physical Review B **99**, 104102 (2019).
 - [44] W. A. Slawinski, H. Y. Playford, S. Hull, S. T. Norberg, S. G. Eriksson, T. Gustafsson, K. Edstrom, and W. R. Brant, Chemistry of Materials **31**, 5024 (2019).
 - [45] I.-K. Jeong and B.-G. Kim, Journal of Applied Physics **126**, 014101 (2019).
 - [46] A. Masadeh, E. Božin, C. Farrow, G. Paglia, P. Juhas, S. Billinge, A. Karkamkar, and M. G. Kanatzidis, Physical Review B **76**, 115413 (2007).
 - [47] B. Toby and T. Egami, Acta Crystallographica Section A: Foundations of Crystallography **48**, 336 (1992).
 - [48] H. Kröncke, S. Figge, D. Hommel, and B. M. Epelbaum, Acta Phys. Pol. A **114**, 1193 (2008).
 - [49] C. Farrow, P. Juhas, J. Liu, D. Bryndin, E. Božin, J. Bloch, T. Proffen, and S. Billinge, Journal of Physics: Condensed Matter **19**, 335219 (2007).
 - [50] A. M. Abeykoon, W. Donner, M. Brunelli, M. Castro-Colin, A. J. Jacobson, and S. C. Moss, Journal of the American Chemical Society **131**, 13230 (2009).
 - [51] OriginPro 2013, *OriginLab Corporation*, Northampton, MA, USA.
 - [52] E. E. McCabe, A. S. Wills, L. Chapon, P. Manuel, and J. S. O. Evans, Phys. Rev. B **90**, 165111 (2014).
 - [53] R. K. Oogarah, C. P. J. Stockdale, C. Stock, J. S. O. Evans, A. S. Wills, J. W. Taylor, and E. E. McCabe, Phys. Rev. B **95**, 174441 (2017).
 - [54] K. Horigane, A. Llobet, and D. Louca, Phys. Rev. Lett. **112**, 097001 (2014).
 - [55] H.-H. Kuo, J.-H. Chu, J. C. Palmstrom, S. A. Kivelson, and I. R. Fisher, Science **352**, 958 (2016).
 - [56] A. E. Bhmer and C. Meingast, Comptes Rendus Physique **17**, 90 (2016).
 - [57] E. P. Rosenthal, E. F. Andrade, C. J. Arguello, R. M. Fernandes, L. Y. Xing, X. C. Wang, C. Q. Jin, A. J. Millis, and A. N. Pasupathy, Nature Physics **10**, 225 (2014).
 - [58] J. Wang, G.-Z. Liu, D. V. Efremov, and J. van den Brink, Phys. Rev. B **95**, 024511 (2017).
 - [59] P. Dai, Rev. Mod. Phys. **87**, 855 (2015).
 - [60] G. R. Stewart, Rev. Mod. Phys. **83**, 1589 (2011).